Industrial Chemistry & Materials

ROYAL SOCIETY OF CHEMISTRY

PAPER

View Article Online
View Journal

Check for updates

Cite this: DOI: 10.1039/d5im00134j

In situ molecular passivation for improved performance and spectral stability in thermally evaporated pure blue perovskite light-emitting diodes

Jiyoung Kwon,[ab] Yunna Kim,[a] Nakyung Kim,[a] Jinu Park,[a] Sukki Lee,[a] Seoyeon Park,[a] Sunwoo Kang *[c] and Byungha Shin *[a]

Received 3rd July 2025,
Accepted 20th August 2025

DOI: 10.1039/d5im00134j

rsc.li/icm

Pure blue perovskite light-emitting diodes (PeLEDs) produced *via* vacuum deposition have limited efficiency and spectral stability due to defect-induced non-radiative recombination and halide migration. In this study, we report a pure blue PeLED with improved performance, featuring a thermally evaporated perovskite layer passivated *in situ* using 4,7-di(9H-carbazol-9-yl)-1,10-phenanthroline (BUPH1), a newly introduced phenanthroline-based small molecule designed to coordinate under-coordinated Pb^{2+} ions. The bidentate coordination of BUPH1 effectively passivates halide vacancies and suppresses ion migration, resulting in improved film morphology, enhanced photoluminescence quantum yield, reduced trap density, and increased exciton binding energy. The optimized perovskite film emits at 472 nm with a narrow full width at half maximum of 19 nm, exhibiting pure blue emission suitable for Recommendation ITU-R BT.2020, an industrial standard for color gamut. The corresponding PeLED achieves an external quantum efficiency of 3.10%, the highest value reported for thermally evaporated pure blue PeLEDs. In addition, the device maintains excellent spectral and color stability under electrical bias, with no noticeable peak shift or change in chromaticity coordinates across varying voltages. This work demonstrates that *in situ* molecular passivation is an effective strategy to overcome key limitations of thermally evaporated perovskite emitters and supports their potential for next-generation high-resolution display technologies.

Keywords: Perovskite light-emitting diodes; Thermal evaporation; Vacuum deposition; Pure blue emission; *In situ* passivation; Spectral stability.

1 Introduction

Metal halide perovskites have emerged as highly attractive candidates for future light-emitting diodes (LEDs) owing to their outstanding optoelectronic properties such as high charge carrier mobility, excellent defect tolerance, tunable bandgap, narrow emission linewidths, and high photoluminescence quantum yield (PLQY).[1–14] These characteristics make them ideally suited for high-definition, wide-color-gamut displays, particularly those targeting the Rec.2020 color standard. Recently, the display industry has shifted from liquid crystal displays (LCDs) to organic light-emitting diodes (OLEDs), driven by the advantages of self-emissive operation, superior image quality, and the ability to cover a wide color gamut.[15] In this context, perovskite-based LEDs (PeLEDs) are gaining attention as a next-generation display technology, combining the intrinsic material advantages of perovskites with the compatibility with the existing OLED fabrication infrastructure.[16–19] Although electroluminescent quantum dot (EL-QD) LEDs were once considered the next generation of displays after OLEDs, they have faced significant commercialization challenges, particularly due to difficulties associated with solution-based processes.[20] Unlike EL-QD LEDs, metal halide perovskites can be processed by vacuum thermal evaporation, which is a mature and widely adopted method for OLED production. This compatibility enables precise thickness control, high-resolution patterning, uniform film formation, and dry processing, offering a scalable and industry-ready route for high-performance devices. Moreover, vacuum deposition eliminates solvent-related issues common in solution

---

[a] Department of Materials Science and Engineering, Korea Advanced Institute of Science and Technology (KAIST), Daejeon 34141, Republic of Korea.
E-mail: byungha@kaist.ac.kr
[b] Samsung Display Co., Yongin-si, Gyeonggi-do 17113, Republic of Korea
[c] Department of Chemistry, Dankook University, Cheonan 31116, Republic of Korea.
E-mail: sunwoo.kang@dankook.ac.kr

processing, such as precursor solubility limitations, solvent incompatibility, and environmental concerns.[21,22] As a result, thermally evaporated PeLEDs represent the practical integration of the advantages of perovskite materials with an established industrial fabrication infrastructure.

Currently, red and green perovskite LEDs fabricated *via* solution processing have external quantum efficiencies (EQEs) exceeding 30%.[23–25] Blue PeLEDs exhibit high efficiencies, with values of 26.4% at 480 nm, 24.3% at 475 nm, and 16.7% at 465 nm.[26] In contrast, thermally evaporated PeLEDs still exhibit relatively lower efficiencies, with EQEs of 12.6% for red, 16.1% for green, 10.41% at 484 nm, and 2.47% at 475 nm.[27–30] This performance gap is primarily attributed to the relatively limited number of studies on thermally evaporated PeLEDs compared with their solution-processed counterparts, indicating the need for further development to enhance device efficiency.[31] In addition, it stems from the formation of unsaturated Pb^{2+} defects during the high-temperature evaporation of precursors, where partial thermal decomposition leads to a halide-deficient growth environment. These defects serve as non-radiative recombination centers, significantly reducing PLQY.[32] In particular, the realization of pure blue emission within the 460–475 nm range remains a critical challenge. According to the CIE 1931 color space, the Rec. 2020 standard defines the optimal blue coordinate as near 468 nm, positioning this spectral region as the most desirable for next-generation display applications. While shorter-wavelength deep blue emissions (<460 nm) can lead to increased visual fatigue, and longer-wavelength sky blue emissions (>475 nm) often fail to deliver vivid color contrast, pure blue offers the best compromise between color purity and visual comfort.[33–35] Despite this importance, pure blue PeLEDs inherently suffer from lower EQE and luminance compared to sky blue counterparts due to the human eye's reduced sensitivity in this spectral range. Moreover, to achieve emission in the pure blue region, a high Cl/Br ratio is typically required, which often results in phase segregation and spectral instability.[36] This makes precise control over the halide composition and emission wavelength particularly challenging in thermally evaporated PeLEDs, further complicating the development of efficient and stable pure blue devices.

In this work, we address the fundamental limitation of thermally evaporated PeLEDs, where unsaturated Pb^{2+} defects formed during high-temperature precursor evaporation act as non-radiative recombination centers. To overcome this, we introduce BUPH1 ($C_{36}H_{22}N_4$, 4,7-di(9*H*-carbazol-9-yl)-1,10-phenanthroline), a phenanthroline-based small molecule compatible with vacuum thermal evaporation. Co-evaporated with the perovskite precursors, BUPH1 enables *in situ* passivation of under-coordinated Pb^{2+} ions through bidentate coordination *via* its nitrogen lone pairs.[37,38] In addition, BUPH1 consists of phenanthroline and carbazole moieties, where phenanthroline exhibits excellent electron transport properties and carbazole facilitates efficient hole transport, thereby contributing to an improved charge balance within the device.[39] This study presents the first application of BUPH1 for passivation of halide perovskite light emitters by introducing the bidentate coordination of a phenanthroline-based compound as a defect passivation strategy. This effectively passivates halide vacancies and suppresses ion migration without requiring additional processing steps. To achieve high color purity in the blue region, we precisely controlled the halide composition by co-evaporating $PbBr_2$, CsCl, and CsBr. This enabled the formation of a mixed-halide perovskite emitting at 472 nm, which closely aligns with the Rec. 2020 pure-blue standard. Leveraging this compositionally tuned perovskite together with the molecular passivation strategy, we demonstrate a high-efficiency pure-blue PeLED fabricated *via* vacuum deposition. The device exhibits an EL peak at 472 nm, a narrow full width at half maximum (FWHM) of 19 nm, and an EQE of 3.10%, which is the highest value reported so far for thermally evaporated pure-blue PeLEDs. These results highlight the synergistic benefits of thermally evaporated perovskite engineering and *in situ* defect passivation in advancing efficient and spectrally stable blue emitters for next-generation display technologies.

2 Results and discussion

The perovskite films were fabricated *via* simultaneous thermal co-evaporation of $PbBr_2$, CsCl, CsBr, and BUPH1 under high vacuum conditions ($<3.0 \times 10^{-6}$ Torr), as schematically illustrated in Fig. S1. BUPH1 is a phenanthroline-based organic molecule featuring two carbazole substituents. The nitrogen atoms in the phenanthroline core of BUPH1 each carry a lone pair of electrons and act as a bidentate ligand, simultaneously coordinating both lone pairs to a single under-coordinated Pb^{2+} ion, as shown in Fig. 1a. This chelation passivates the halide vacancy sites in the perovskite lattice by binding to under-coordinated Pb^{2+} ions that are left unbonded due to halide vacancies and structural defects, thereby saturating the defect sites.[40] As a result, passivation effectively prevents spectral shifts and instability while suppressing non-radiative recombination pathways.

As shown in Fig. 1b, the PL spectra reveal the evolution of the optical properties across the three-step compositional modification. The initial film composed of $PbBr_2$ and CsCl (deposition rate: $PbBr_2$ 0.5 Å s^{-1}, CsCl 0.65 Å s^{-1}) exhibits a PL emission peak centered at 467.5 nm. The Br/Cl ratio determined by the flux rate is 1.5, leading to the formation of $CsPbBr_{1.8}Cl_{1.2}$. The observed emission peak at 467.5 nm corresponds to a bandgap of 2.65 eV, which is higher than the reported bandgap.[41] This is likely due to the quantum confinement effects induced by the presence of the zero-dimensional (0D) perovskite $Cs_4PbBr_xCl_{6-x}$ which results in a spectral blue shift and an apparently larger calculated bandgap.[42] It also exhibits a relatively broad FWHM of 24.9 nm, and low PLQY of 5.1%, indicating poor color purity and dominant non-radiative recombination. Upon introducing

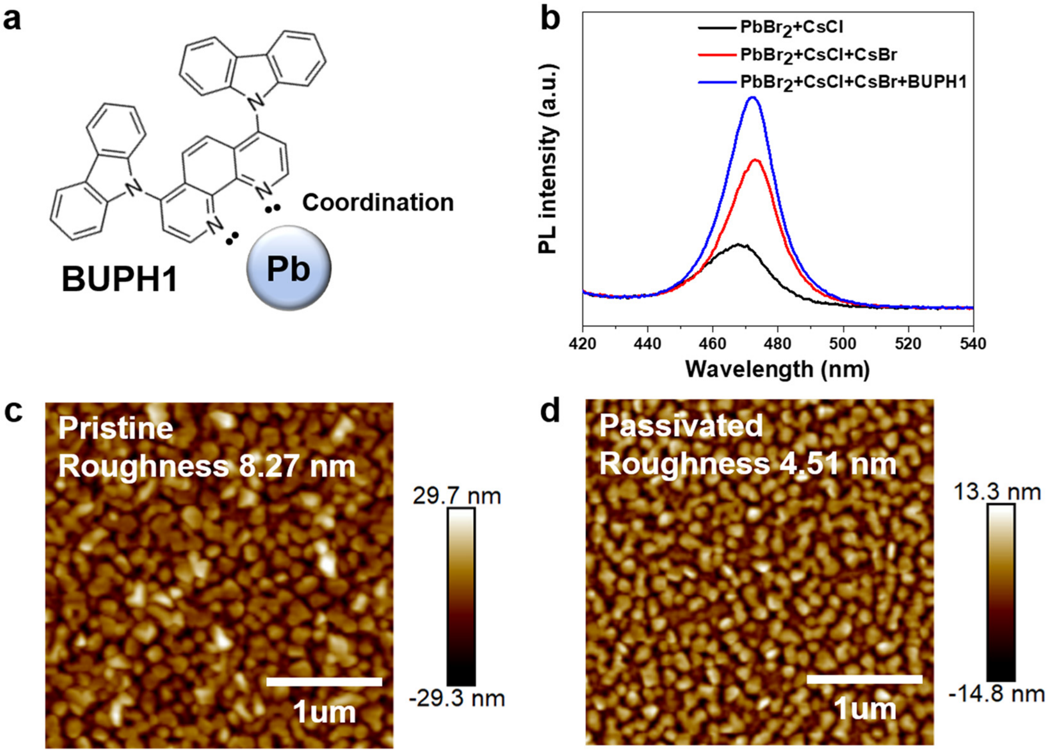

Fig. 1 Overview of the passivation effects of BUPH1. (a) Schematic of bidentate coordination between BUPH1 and under-coordinated Pb^{2+} ions; (b) PL spectra showing emission redshift, PLQY enhancement, and FWHM narrowing with CsBr and BUPH1; AFM images of (c) pristine and (d) BUPH1-passivated films.

CsBr into the system (deposition rate: 0.3 Å s^{-1}), the emission peak redshifts to 472 nm due to increased bromide content, and the formation of 0D perovskite $Cs_4PbBr_xCl_{6-x}$ is promoted, leading to an increase in PLQY to 7.9% as a result of quantum confinement effects.[42,43] Finally, by introducing the molecular passivation agent BUPH1 to implement a 4-component co-deposition system, the PLQY is enhanced to 16.2% and the FWHM is narrowed to 18.3 nm. These enhancements indicate that BUPH1 effectively reduces trap-assisted recombination and improves radiative efficiency by passivating vacancies and defects, thereby leading to spectrally pure and efficient emission (Table S1). According to atomic force microscopy (AFM) analysis (Fig. 1c and d), the surface roughness of the pristine $CsPbBr_xCl_{3-x}$ film formed by 3-component co-deposition decreases from 8.27 nm to 4.51 nm after BUPH1 incorporation, resulting in a smoother and more uniform morphology, along with grain size reduction (Fig. S2). This suggests that the passivation effect, driven by coordination interactions between BUPH1 and Pb^{2+} ions, suppresses the crystal growth rate and promotes uniform nucleation across the substrate, leading to controlled grain growth during film formation. Furthermore, grazing-incidence X-ray diffraction (GIXRD) patterns (Fig. S3) validate the improved crystallinity and enhanced structural ordering of the BUPH1-treated films. In particular, the (100) diffraction peak at 15.6° becomes sharper and more intense, indicating that random crystal growth is suppressed and preferential orientation along the (100) plane is promoted compared to pristine perovskite films. The (100) plane is known to exhibit favorable charge transport properties and low defect density, which can enhance the device performance.[44,45]

The incorporation and distribution of BUPH1 within perovskite films were examined using time-of-flight secondary ion mass spectrometry (ToF-SIMS). As shown in Fig. 2a, the depth profiles of Cs^-, Pb^-, Br^-, and Cl^- exhibit stable intensities across the sputtering time, indicating uniform elemental composition throughout the film deposited on a Si substrate. Notably, the CN^- ion, which are characteristic fragment of BUPH1, were detected throughout the film depth, validating the successful incorporation and homogeneous distribution of BUPH1 within the perovskite matrix. As shown in Fig. S4, the intensity of the CN^- signal increases with the BUPH1 deposition rate, confirming dose-dependent incorporation. In addition, ellipsometry measurements on a BUPH1-only film deposited at 0.01 Å s^{-1} for 60 minutes revealed a film thickness of 5.74 nm, as fitted using the Cauchy model (Fig. S5), confirming the consistency of the intended deposition rates.[46]

To check the potential passivation role of the BUPH ligand, density functional theory (DFT) calculations were performed. As shown in Fig. 2b, the BUPH ligand bidentately coordinates to the Pb site at a distance of 3.5 Å. In the optimized structure, the adsorption energy of BUPH ligand was calculated to be 0.200 eV, which may be sufficient to play as the passivation role in enhancing the perovskite stability.[47]

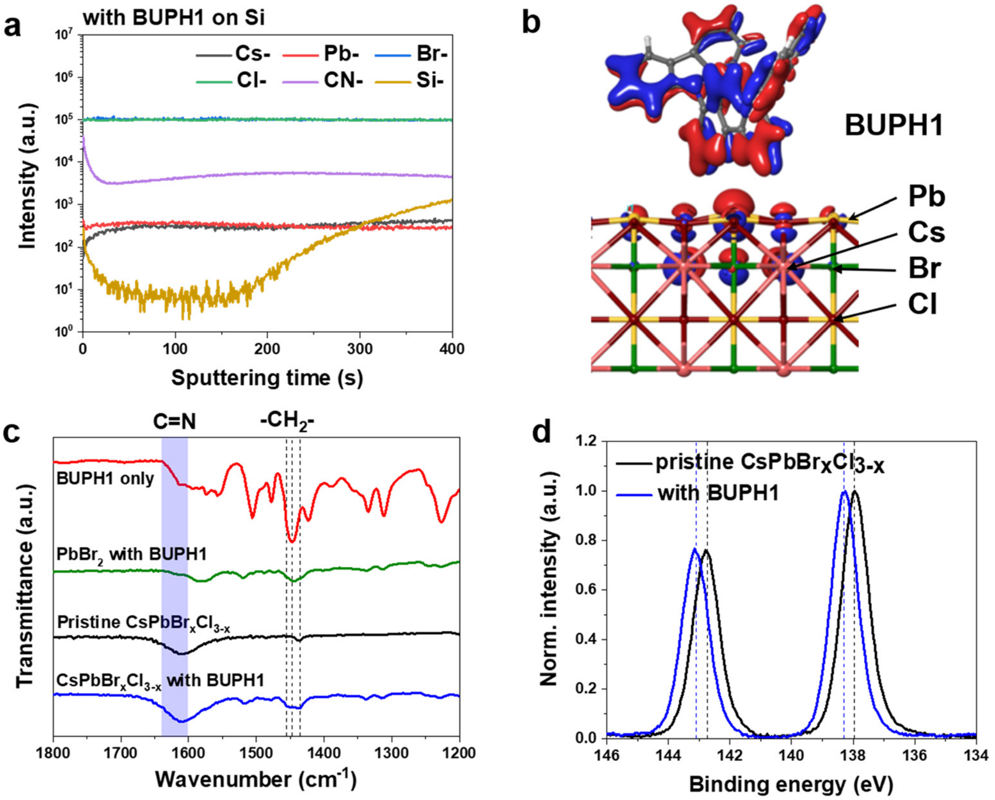

Fig. 2 Evidence of BUPH1 incorporation and coordination in perovskite films. (a) ToF-SIMS depth profiles showing the uniform distribution of Cs, Pb, Br, Cl, and CN (from BUPH1); (b) optimized structure of BUPH1 adsorbed $CsPbBr_xCl_{3-x}$ and corresponding charge density distribution (Pb: yellow, Cs: pink, Br: green, Cl: red); (c) FT-IR spectra showing CH_2 scissoring shift and enhanced C═N absorption, indicating Pb^{2+}–BUPH1 coordination; (d) Pb 4f XPS spectra with +0.35 eV shift upon BUPH1 addition.

Experimental evidence for BUPH1–Pb^{2+} coordination was obtained using Fourier-transform infrared (FT-IR) spectroscopy (Fig. 2c). In the pristine BUPH1 film, a distinct $-CH_2-$ scissoring vibration peak appears at approximately 1447 cm^{-1}. After incorporation into the perovskite lattice (BUPH1-passivated perovskite), the original peak at 1447 cm^{-1} is no longer observed, while two nearby peaks appear at 1430 cm^{-1} and 1457 cm^{-1}. The peak at 1430 cm^{-1} originates from intrinsic vibrational modes of the pristine perovskite itself, while the new peak at 1457 cm^{-1} corresponds to a shifted form of the original BUPH1 peak at 1446 cm^{-1}. This shift indicates a modification of the vibrational environment around the $-CH_2-$ groups due to the coordination of Pb^{2+} ions with nitrogen atoms in the phenanthroline moiety of BUPH1. In contrast, in the $PbBr_2$ with BUPH1 film, the 1446 cm^{-1} peak remains unchanged, suggesting that no significant vacancy sites exist around Pb^{2+} ions in $PbBr_2$, thereby preventing coordination with BUPH1. Furthermore, the characteristic C═N vibration typically located between 1600–1650 cm^{-1} overlaps with the intrinsic perovskite peaks, leading to a significant absorption peak in the passivated perovskite spectrum. An X-ray photoelectron spectroscopy (XPS) analysis of Pb 4f peaks (Fig. 2d) further supports these findings: the Pb $4f_{5/2}$ and $4f_{7/2}$ peaks in BUPH1-passivated perovskite films exhibit a binding energy shift of approximately +0.35 eV relative to the pristine sample. This shift is attributed to changes in the electronic environment of Pb^{2+} ions upon coordination with the nitrogen atoms in the phenanthroline moiety of BUPH1.

The optical properties of the perovskite films were systematically investigated using power-dependent PL, time-resolved PL (TR-PL), and temperature-dependent PL (TD-PL) measurements. As shown in Fig. 3a, the BUPH1-passivated films exhibited enhanced PLQY across the entire range of excitation power, indicating improved radiative recombination efficiency due to trap state suppression. At low excitation densities, the PLQY increases as trap states become filled, whereas at high excitation levels, Auger recombination dominates, resulting in a decrease in PLQY.[48,49] To further understand the impact of BUPH1 on carrier dynamics, a TR-PL analysis was conducted (Fig. 3b, Table S2). The average PL lifetime (τ_{av}) increased from 7.54 ns in pristine films to 11.58 ns in the BUPH1-treated films. Based on biexponential fitting of the TR-PL decay curves, the proportion of radiative recombination increased from 61.6% to 80.5%, while the non-radiative component decreased from 38.4% to 19.5% after BUPH1 passivation. Notably, while the radiative lifetime (τ_{rad}) decreased from 95.49 ns to 71.48 ns, the non-radiative lifetime ($\tau_{non\text{-}rad}$) significantly increased from 8.19 ns to 13.82 ns, confirming that defect-assisted

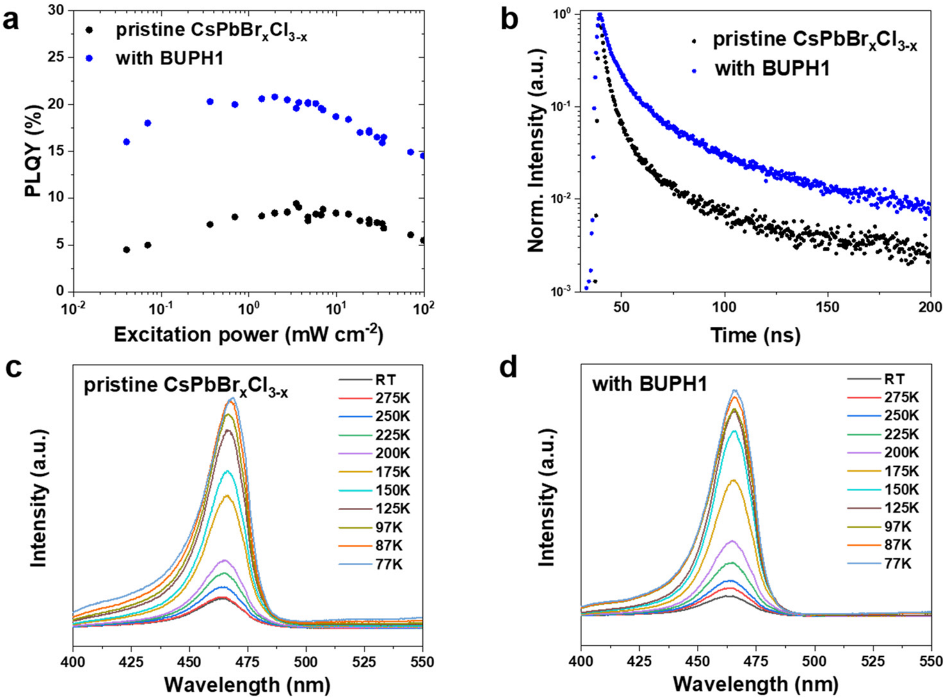

Fig. 3 Optical characterization of pristine and BUPH1-passivated perovskite films. (a) Power-dependent PLQY showing enhanced efficiency with BUPH1; (b) TR-PL decay indicating longer lifetime and improved radiative recombination; TD-PL spectra of (c) pristine and (d) BUPH1-passivated films.

recombination was effectively suppressed by BUPH1 passivation. These values of Table S2, calculated using equation in Note S2, were derived based on the measured PLQY and average PL lifetimes, enabling a quantitative analysis of the recombination dynamics. This verifies that BUPH1 effectively suppresses defect-mediated recombination and enhances exciton radiative decay pathways.[50] To quantify the exciton binding energy (E_b), temperature-dependent PL spectra were measured from 298 K to 77 K. As shown in Fig. 3c and d, both pristine and BUPH1-passivated films exhibit a gradual increase in PL intensity with decreasing temperature, reflecting the suppression of thermally activated non-radiative recombination. To extract E_b quantitatively, the integrated PL intensity was fitted as a function of the inverse temperature ($1/T$) using the Arrhenius equation below.

$$I(T) = \frac{I_0}{1 + A\cdot\exp\left(-\frac{E_b}{kT}\right)}$$

where $I(T)$ is the PL intensity at temperature T, I_0 is the intensity at 0 K, A is a fitting constant, k is the Boltzmann constant, and E_b is the exciton binding energy. From the fitting results shown in Fig. S6, the BUPH1-passivated film exhibited an E_b of 78.0 meV, which is higher than that of the pristine film (56.2 meV). This enhancement is caused by enhanced dielectric and spatial confinement effects, which result from the reduced grain size and improved film uniformity.[51]

Fig. 4a illustrates the device architecture, which consists of a multilayer stack in the following order: ITO/PEDOT:PSS/TFB:F4-TCNQ/perovskite/TPBi/LiF/Al. The corresponding energy level diagram is presented in Fig. 4b. The energy levels of the perovskite layer remain unchanged regardless of BUPH1 passivation, with the highest occupied molecular orbital (HOMO) positioned at 5.35 eV and the lowest unoccupied molecular orbital (LUMO) at 2.85 eV, resulting in an optical bandgap (E_g) of 2.5 eV. The HOMO level was determined by ultraviolet photoelectron spectroscopy (UPS, Fig. S7), while the optical bandgap was estimated from the Tauc plot of the UV-vis absorption spectrum (Fig. S8). To achieve efficient energy level alignment TFB (poly[(9,9-dioctylfluorenyl-2,7-diyl)-*co*-(4,4′-(*N*-(4-*sec*-butylphenyl)diphenylamine)]) was selected as the hole transport layer (HTL). To further enhance hole injection and transport, TFB was p-doped with 3 wt% of F4-TCNQ ($C_{12}F_4N_4$, 2,3,5,6-tetrafluoro-7,7,8,8-tetracyanoquinodimethane), an electron acceptor known to effectively increase hole density *via* charge transfer complex formation.[52]

The reproducibility of device performance was assessed across 20 individual devices in Fig. 4c, and the histogram is presented in Fig. S9. Fig. 4d presents the EQE characteristics of the devices as a function of current density. The pristine device exhibits a peak EQE of 1.62%, while the BUPH1-passivated device achieves a significantly enhanced maximum EQE of 3.10%, attributed to the effective passivation of non-radiative defect sites by BUPH1. This EQE of 3.10% represents the highest value reported to date for thermally evaporated pure blue perovskite LEDs (see also Fig.

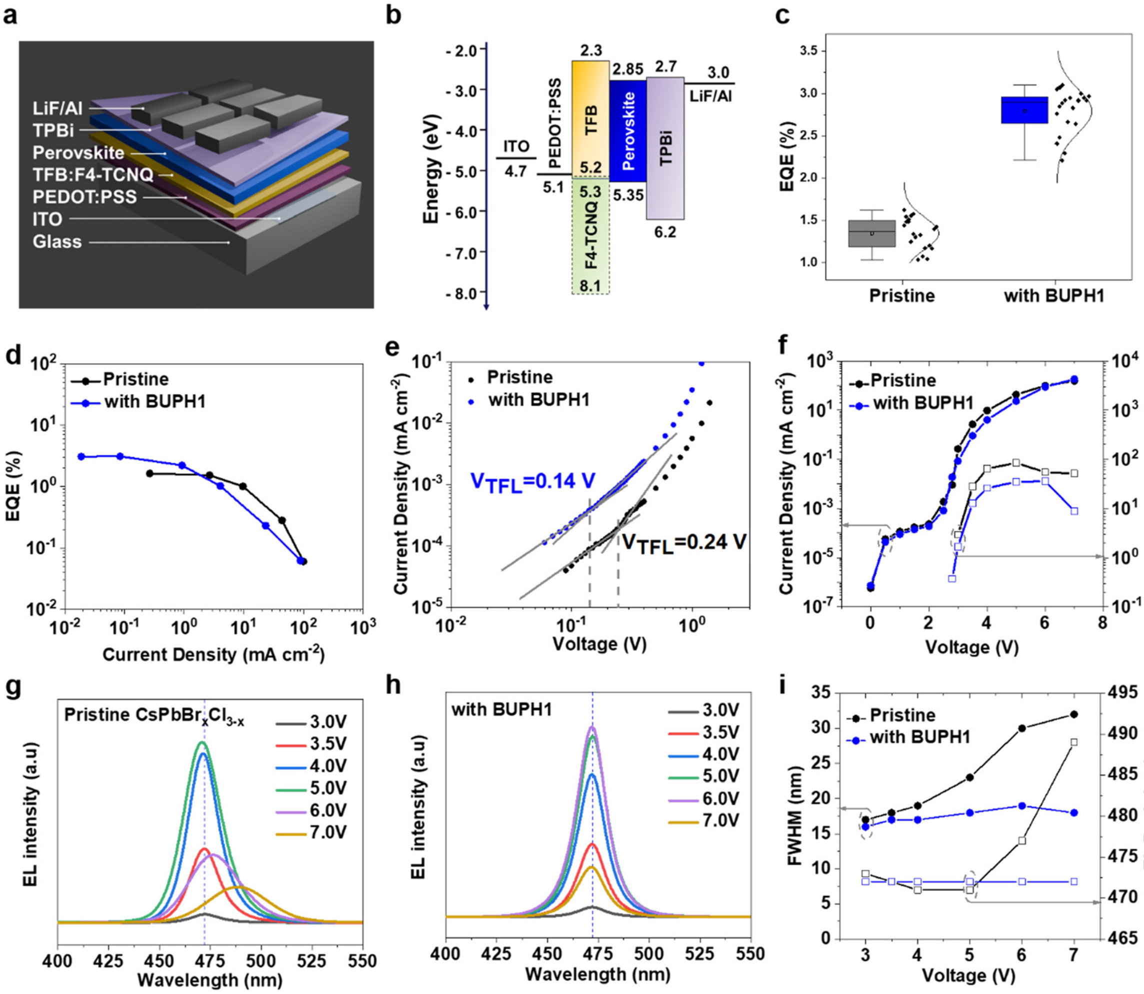

Fig. 4 Device structure and performance. (a) PeLED architecture; (b) energy levels showing unchanged perovskite HOMO/LUMO after passivation; (c) statistical distribution of peak EQE values measured from 20 devices; (d) current density dependent EQE curves; (e) hole-only *J*–*V* curves; (f) *J*–*V*–*L* characteristics; EL spectra of (g) pristine and (h) BUPH1-passivated devices; (i) summary of the voltage-dependent EL spectra.

S10, Table S3). Passivation is a key strategy for blue perovskites, and various additives have been employed for this purpose, as summarized in Table S4. Fig. 4e shows the current density–voltage (*J*–*V*) characteristics of the hole-only devices (HODs) with the configuration ITO/PEDOT:PSS/TFB:F4-TCNQ/perovskite/HATCN/Al.[53] From these curves, the trap-filled limit voltage (VTFL) was extracted to be 0.24 V for the pristine perovskite and 0.14 V for the BUPH1-passivated film. The corresponding trap densities (N_t) were calculated using the following equation:

$$N_t = \frac{2\varepsilon_r \varepsilon_0 V_{\mathrm{TFL}}}{eL^2}$$

where ε_r is the relative dielectric constant of the perovskite (3.44), ε_0 is the vacuum permittivity (8.854 × 10^{-14} F cm^{-1}), *e* is the electron charge (1.602 × 10^{-19} C), and *L* is the perovskite film thickness (40 nm).[29] Based on this equation, the calculated trap density decreased from 5.70 × 1016 cm^{-3} in the pristine film to 3.33 × 1016 cm^{-3} after BUPH1 passivation, demonstrating the effective suppression of trap states. A similar trend was observed in electron-only devices (EODs) with the configuration ITO/TPBi/perovskite/TPBi/LiF/Al,[54] where N_t was reduced from 3.09 × 1016 cm^{-3} to 2.61 × 1016 cm^{-3} (Fig. S11). Complementary to this experimental evidence, density of states (DOS) calculations (Fig. S12) revealed that BUPH adsorption suppresses the shallow trap states near the band edges, resulting in a more defined electronic structure. As shown in Fig. S13, the matching *J*–*V* curves of the HOD and EOD indicate that the passivated device exhibits improved charge balance. Furthermore, in the trap-free space-charge-limited current (SCLC) regime of single-carrier devices, the charge carrier mobilities were extracted using the Mott–Gurney law.

$$\mu = \frac{8}{9}\frac{JL^3}{\varepsilon_r \varepsilon_0 V^2}$$

where *J* and *V* were obtained from the region where the slope of the log*J*–log*V* plot was approximately 2 (Fig. S14). The pristine device exhibited a hole mobility of $\mu_h = 6.56 \times 10^{-10}$ $cm^2 V^{-1} s^{-1}$ and an electron mobility of $\mu_e = 9.58 \times 10^{-10}$ $cm^2 V^{-1} s^{-1}$, resulting in a ratio (μ_e/μ_h) of 1.46. For the device with BUPH1, the mobilities were improved, with $\mu_h = 2.78 \times 10^{-9}$ $cm^2 V^{-1} s^{-1}$ and $\mu_e = 2.53 \times 10^{-9}$ $cm^2 V^{-1} s^{-1}$, yielding an improved balanced ratio of 0.91. This enhancement is attributed to the increased current levels for both holes and electrons by passivated trap state. Notably, the improvement in hole current due to the mitigation of hole traps is more pronounced than the enhancement on the electron side, thereby contributing to improved injection balance from both charge transport layers. Consequently, the suppression of non-radiative recombination caused by excess charges further contributes to the improvement in device efficiency. Fig. 4f displays the current density–voltage–luminance (*J–V–L*) characteristics of the devices. Trap-induced non-radiative recombination increases the leakage current, resulting in a higher injection current density in the pristine PeLED.[55] Although the BUPH1-passivated device exhibits relatively low luminance, this work achieves the narrowest emission linewidth (FWHM = 19 nm) among all reported thermally evaporated blue PeLEDs to date. Given that luminance is proportional to the integrated area under the EL spectrum, the narrow spectral width inherently limits overall brightness.[56] This trade-off underscores the need for further optimization of charge injection and device architecture to enhance luminance while preserving high color purity.

When an electric field is applied to the pristine device, the EL spectrum exhibits a notable red-shift due to halide migration, as shown in Fig. 4g. In contrast, the device passivated with BUPH1 displays a stable spectral behavior without any noticeable peak shift under varying voltages, as demonstrated in Fig. 4h. Fig. 4i summarizes the voltage-dependent evolution of the EL spectrum. For the pristine perovskite LED, the emission peak shifts from 473 nm at 3 V to 489 nm at 7 V. However, the BUPH1-passivated device maintains a consistent peak position at 472 nm across the entire voltage range. Furthermore, FWHM remains stable, increasing only slightly from 16 nm at 3 V to 19 nm at 7 V, indicating effective suppression of spectral broadening by BUPH1 passivation. Fig. S15 presents the CIE chromaticity coordinates of the devices at different operating voltages. The pristine device exhibits a clear shift toward the green region as the voltage increases, indicating spectral instability. In contrast, the BUPH1-passivated device maintains highly stable color coordinates with negligible variation across the entire voltage range, highlighting its superior spectral stability under electrical bias.

Fig. S16 show the operational lifetime of the PeLEDs measured at an initial luminance of 10 cd m^{-2}. The BUPH1-passivated device exhibited a T_{50} lifetime of 20 s under constant current driving conditions, indicating a relative improvement in stability compared with its pristine counterpart. The peak wavelength and FWHM remained stable during operation, demonstrating excellent spectral stability (Fig. S17). However, the overall lifetime remained short, and the presence of metallic Pb^0 was identified in a Pb 4f XPS analysis after device operation (Fig. S18). This was attributed to the degradation and lack of effective passivation caused by device aging.[57] These findings suggest that further optimization and introduction of additional passivation materials are required in future studies. In addition, while the current study focused on the thermal evaporation of the emissive layer and passivation agent, future efforts should identify vacuum-deposable HTL materials for all thermally evaporated PeLEDs that provide optimal energy alignment and charge balance with perovskite emitters.[58]

3 Conclusions

In summary, we demonstrated the performance improvement of a pure blue perovskite LED fabricated entirely *via* vacuum thermal co-evaporation by introducing a novel *in situ* molecular passivation strategy using BUPH1. The phenanthroline-based BUPH1 molecule, introduced here for the first time as a passivation agent, effectively coordinated with under-coordinated Pb^{2+} ions through bidentate binding, passivating halide vacancies and suppressing ion migration. This passivation led to significant improvements in film morphology, crystallinity, and optoelectronic properties, including enhanced PLQY, reduced trap density, increased exciton binding energy, and prolonged carrier lifetimes. The resulting PeLED device emits at 472 nm with a narrow FWHM of 19 nm and achieved an EQE of 3.10%. This value is the highest reported to date for thermally evaporated pure blue perovskite LEDs. Moreover, the device exhibited remarkable spectral and color stability under electrical bias, with no observable EL peak shift and negligible changes in CIE coordinates across a range of operating voltages. These findings provide a practical solution to overcome defect-related limitations in thermally evaporated PeLEDs and lay the foundation for the future development of full-color perovskite display technologies. Further optimization of charge injection and device architecture will be essential for achieving even higher performance while maintaining spectral integrity.

4 Experimental section

4.1 Materials

$PbBr_2$ (99.999%), CsCl (99.999%), CsBr (99.999%) were purchased from Sigma-Aldrich. Poly(3,4-ethylenedioxythiophene)-poly(styrenesulfonate) (PEDOT:PSS, AI 4083, Heraeus). 4,7-Di(9*H*-carbazol-9-yl)-1,10-phenanthroline (BUPH1, Lumtec), poly[(9,9-dioctylfluorenyl-2,7-diyl)-*co*-(4,40-(*N*-(4-*sec*-butylphenyl)diphenylamine)] (TFB, EMNI), 1,3,5-tris(1-phenyl-1*H*-benzimidazol-2-yl)benzene (TPBi, Lumtec), 2,3,5,6-tetrafluoro-7,7,8,8-tetracyano-quinodimethane (F4-TCNQ, Lumtec), lithium fluoride (LiF), aluminum (Al). All materials were used without any further processing.

4.2 Perovskite film deposition

The perovskite film was fabricated by thermal co-evaporation of $PbBr_2$, CsCl, CsBr, and BUPH1 under high vacuum ($<3 \times 10^{-6}$ Torr). The deposition rates for $PbBr_2$, CsCl, CsBr and BUPH1 were set to 0.5 Å s^{-1}, 0.65 Å s^{-1}, 0.3 Å s^{-1} and 0.01 Å s^{-1}, respectively. After deposition, the film was thermally annealed at 100 °C for 7 minutes. The deposition rates of $PbBr_2$, CsCl, and CsBr were optimized based on the PL peak position and PLQY (Note S3, Fig. S19), and the X-ray photoelectron spectroscopy (XPS) results of the film are presented in Note S4, Table S5, and Fig. S20. The deposition rate of BUPH1 was optimized by considering both PL and EL characteristics (Note S5, Table S6).

4.3 Perovskite LED fabrication

ITO-patterned glass substrates were sequentially cleaned by ultrasonication in deionized water, acetone, and isopropyl alcohol, followed by UV–ozone treatment for 20 minutes. A PEDOT:PSS aqueous solution was spin-coated onto the cleaned substrates at 4000 rpm for 40 seconds and annealed at 150 °C for 30 minutes. A hole transport layer composed of TFB doped with F4-TCNQ was subsequently spin-coated at 2000 rpm for 50 seconds. The substrates were then transferred into a vacuum thermal evaporator, where a 40 nm-thick perovskite film was deposited *via* co-evaporation. Following this, TPBi (40 nm), LiF (1 nm), and Al (100 nm) layers were sequentially deposited under high vacuum ($<3 \times 10^{-6}$ Torr). The effective emission area of the PeLEDs was defined by the overlap between the ITO and Al electrodes, measuring 5 mm^2.

4.4 Perovskite film and device characterization

The surface morphology of the perovskite films was analyzed using atomic force microscopy (AFM, Bruker) in tapping mode. Photoluminescence (PL) spectra and absolute photoluminescence quantum yield (PLQY) were measured using a spectrofluorometer system (Hamamatsu Photonics) equipped with an integrating sphere. Time-resolved photoluminescence (TR-PL) measurements were performed using a fluorescence lifetime system (Horiba) with 374 nm pulsed laser excitation to evaluate carrier recombination dynamics. Temperature-dependent PL (TD-PL) measurements were conducted under vacuum using a closed-cycle helium cryostat, with the temperature varied from 298 K to 77 K. Ultraviolet-visible (UV-vis) absorption spectra were measured using a UV-1800 spectrophotometer (Shimadzu). X-ray photoelectron spectroscopy (XPS, Thermo Scientific) was employed to analyze elemental composition and binding energy shifts. Fourier-transform infrared (FT-IR) spectra were acquired using a Thermo Scientific system to confirm molecular interactions between BUPH1 and the perovskite matrix. Time-of-flight secondary ion mass spectrometry (ToF-SIMS, ION-TOF GmbH) was used for depth profiling of elemental and molecular fragments across the film. The current density–voltage–luminance (*J*–*V*–*L*) characteristics and electroluminescence (EL) spectra of the PeLEDs were measured using a Keithley 2635A source meter coupled with a CS-2000 spectroradiometer (Konica Minolta). The AFM, TR-PL, TD-PL, XPS, FT-IR, and ToF-SIMS analyses were conducted at the KAIST Analysis Center for Research Advancement (KARA).

Author contributions

Jiyoung Kwon: conceptualization, data curation, formal analysis, investigation, methodology, validation, visualization, writing – original draft, writing – review & editing. Yunna Kim: data curation, formal analysis, methodology, validation. Nakyung Kim: formal analysis, methodology. Jinu Park: conceptualization. Sukki Lee: formal analysis. Seoyeon Park: data curation. Sunwoo Kang: software, conceptualization, formal analysis, writing – review & editing. Byungha Shin: funding acquisition, project administration, resources, supervision, writing – review & editing.

Conflicts of interest

The authors declare no conflict of interest.

Data availability

Supplementary information is available: The SI provides additional experimental details, structural and optical characterizations, device statistics, transport analyses, computational data, and figures and tables comparing device performance with previous literature for vacuum thermal evaporated blue PeLEDs. See DOI: **https://doi.org/10.1039/D5IM00134J**.

The data that support the findings of this study are available from the corresponding author upon reasonable request.

Acknowledgements

This work was supported by the National Research Foundation of Korea (NRF) grant funded by the Korea government (MSIT) (RS-2022-NR068162, RS-2023-00208832).

References

1 C. Wehrenfennig, G. E. Eperon, M. B. Johnston, H. J. Snaith and L. M. Herz, High charge carrier mobilities and lifetimes in organolead trihalide perovskites, *Adv. Mater.*, 2013, **26**, 1584.

2 Z.-K. Tan, R. S. Moghaddam, M. L. Lai, P. Docampo, R. Higler, F. Deschler, M. Price, A. Sadhanala, L. M. Pazos, D. Credgington, F. Hanusch, T. Bein, H. J. Snaith and R. H. Friend, Bright light-emitting diodes based on organometal halide perovskite, *Nat. Nanotechnol.*, 2014, **9**, 687–692.

3 H. Cho, S.-H. Jeong, M.-H. Park, Y.-H. Kim, C. Wolf, C.-L. Lee, J. H. Heo, A. Sadhanala, N. Myoung, S. Yoo, S. H. Im, R. H. Friend and T.-W. Lee, Overcoming the

electroluminescence efficiency limitations of perovskite light-emitting diodes, *Science*, 2015, **350**, 1222–1225.

4 T.-H. Han, K. Y. Jang, Y. Dong, R. H. Friend, E. H. Sargent and T.-W. Lee, A roadmap for the commercialization of perovskite light emitters, *Nat. Rev. Mater.*, 2022, **7**, 757–777.

5 X.-Z. Li, Y. Ye, Y. Cao, D. Zhang, Y. Lin, J. Chang, L. Zhu, N. Wang, W. Huang and J. Wang, Tin-halide perovskites for light-emitting diodes, *Chem. Soc. Rev.*, 2025, **54**, 6697–6725.

6 C. Cho, B. Zhao, G. D. Tainter, J.-Y. Lee, R. H. Friend, D. Di, F. Deschler and N. C. Greenham, The role of photon recycling in perovskite light-emitting diodes, *Nat. Commun.*, 2020, **11**, 611.

7 S. Ji, S. R. Bae, L. Hu, A. T. Hoang, M. J. Seol, J. Hong, A. K. Katiyar, B. J. Kim, D. Xu, S. Y. Kim and J.-H. Ahn, Perovskite light-emitting diode display based on MoS_2 backplane thin-film Transistors, *Adv. Mater.*, 2024, **36**, 2309531.

8 Y.-C. Huang, S.-W. Huang, C.-F. Li, S.-H. Huang, F.-Y. Tsai and W.-F. Su, A comprehensive optimization of highly efficient MA-free wide-bandgap perovskites for 4-T perovskite/silicon tandem solar cells, *Chem. Eng. J.*, 2025, **503**, 158272.

9 M. Shin, H. S. Lee, Y. C. Sim, Y.-H. Cho, K. C. Choi and B. Shin, Modulation of growth kinetics of vacuum-deposited CsPbBr3 films for efficient light-emitting diodes, *ACS Appl. Mater. Interfaces*, 2019, **12**, 1944–1952.

10 S. Dutta, J. H. Yoo, S. B. Kwon, S. Panchanan, H. C. Yoo and D. H. Yoon, Green synthesis of Ce doped Cs_3MnBr_5 for highly stable violet light emitting diodes, *Electron. Mater. Lett.*, 2023, **19**, 518–526.

11 J. S. Kim, J.-M. Heo, G.-S. Park, S.-J. Woo, C. Cho, H. J. Yun, D.-H. Kim, J. Park, S.-C. Lee, S.-H. Park, E. Yoon, N. C. Greenham and T.-W. Lee, Ultra-bright, efficient and stable perovskite light-emitting diodes, *Nature*, 2022, **611**, 688–694.

12 Y.-H. Kim, J. Park, S. Kim, J. S. Kim, H. Xu, S.-H. Jeong, B. Hu and T.-W. Lee, Exploiting the full advantages of colloidal perovskite nanocrystals for large-area efficient light-emitting diodes, *Nat. Nanotechnol.*, 2022, **17**, 590–597.

13 I. Mosquera-Lois, Y.-T. Huang, H. Lohan, J. Ye, A. Walsh and R. L. Hoye, Multifaceted nature of defect tolerance in halide perovskites and emerging semiconductors, *Nat. Rev. Chem.*, 2025, **9**, 287–304.

14 H. Yoon, S. Hong, S. H. Lee, I. H. Cho and H. J. Kim, GIWAXS analysis on preferred orientation in metal halide perovskite films via alkylamines, *Electron. Mater. Lett.*, 2022, **18**, 456–464.

15 H.-W. Chen, J.-H. Lee, B.-Y. Lin, S. Chen and S.-T. Wu, Liquid crystal display and organic light-emitting diode display: Present status and future perspectives, *Light:Sci. Appl.*, 2018, **7**, 17168–17168.

16 Y. Huang, J. Zhu, J. Li, J. Luo, P. Du, B. Song and J. Tang, Thermally evaporated blue quasi-two-dimensional perovskite light-emitting diodes via low-dimensional phase distribution arrangement, *ACS Appl. Mater. Interfaces*, 2024, **16**, 15004–15010.

17 Z. Y. He, C. C. Peng, R. D. Guo, B. Chen, X. Li, X. Y. Zhu, J. Zhang, W. X. Liang and L. Wang, High-efficiency and emission-tunable inorganic blue perovskite light-emitting diodes based on vacuum deposition, *Small*, 2024, **20**, 2305379.

18 P. Du, J. Li, L. Wang, J. Liu, S. Li, N. Liu, Y. Li, M. Zhang, L. Gao, Y. Ma and J. Tang, Vacuum-deposited blue inorganic perovskite light-emitting diodes, *ACS Appl. Mater. Interfaces*, 2019, **11**, 47083–47090.

19 N. Kim, M. Shin, S. Jun, B. Choi, J. Kim, J. Park, H. Kim, W. Jung, J.-Y. Lee, Y.-H. Cho and B. Shin, Highly efficient vacuum-evaporated $CsPbBr_3$ perovskite light-emitting diodes with an electrical conductivity enhanced polymer-assisted passivation layer, *ACS Appl. Mater. Interfaces*, 2021, **13**, 37323–37330.

20 H. Li, J. Zhang, W. Wen, Y. Zhao, H. Gao, B. Ji, Y. Wang, L. Jiang and Y. Wu, Highly efficient light-emitting diodes via self-assembled InP quantum dots, *Nat. Commun.*, 2025, **16**, 4257.

21 C. Peng, Z. He, R. Guo, X. Li, B. Chen, L. Sun and L. Wang, The synergy of pre-frozen substrates and post-annealing for high-efficiency co-evaporated blue perovskite LEDs, *Chem. Eng. J.*, 2024, **493**, 152579.

22 C. Peng, B. Chen, X. Liu, R. Guo, Z. He, F. Zhang, X. He, L. Sun, Z. Liu, Y. Xiong, F. Gao and L. Wang, High-performance thermally evaporated blue perovskite light-emitting diodes enabled by post-evaporation passivation, *Chem. Eng. J.*, 2024, **499**, 155955.

23 S. C. Feng, Y. Shen, X. M. Hu, Z. H. Su, K. Zhang, B. F. Wang, L. X. Cao, F. M. Xie, H. Z. Li, X. Gao, J.-X. Tang and Y.-Q. Li, Efficient and stable red perovskite light-emitting diodes via thermodynamic crystallization control, *Adv. Mater.*, 2024, **36**, 2410255.

24 W. Bai, T. Xuan, H. Zhao, H. Dong, X. Cheng, L. Wang and R. J. Xie, Perovskite light-emitting diodes with an external quantum efficiency exceeding 30%, *Adv. Mater.*, 2023, **35**, 2302283.

25 S. Q. Sun, J. W. Tai, W. He, Y. J. Yu, Z. Q. Feng, Q. Sun, K. N. Tong, K. Shi, B. C. Liu, M. Zhu, G. Wei, J. Fan, Y.-M. Xie, L.-S. Liao and M.-K. Fung, Enhancing light outcoupling efficiency via anisotropic low refractive index electron transporting materials for efficient perovskite light-emitting diodes, *Adv. Mater.*, 2024, **36**, 2400421.

26 Y. Gao, Q. Cai, Y. He, D. Zhang, Q. Cao, M. Zhu, Z. Ma, B. Zhao, H. He, D. Di, Z. Ye and X. Dai, Highly efficient blue light-emitting diodes based on mixed-halide perovskites with reduced chlorine defects, *Sci. Adv.*, 2024, **10**, eado5645.

27 N. Liu, Z. Liu, Y. Huang, P. Du, X. Zhang, Y. Leng, J. Luo, J. Du and J. Tang, Fluorine-modified passivator for efficient vacuum-deposited pure-red perovskite light-emitting diodes, *Light:Sci. Appl.*, 2025, **14**, 118.

28 J. Li, P. Du, Q. Guo, L. Sun, Z. Shen, J. Zhu, C. Dong, L. Wang, X. Zhang, L. Li, C. Yang, J. Pan, Z. Liu, B. Xia, Z. Xiao, J. Du, B. Song, J. Luo and J. Tang, Efficient all-thermally evaporated perovskite light-emitting diodes for active-matrix displays, *Nat. Photonics*, 2023, **17**, 435–441.

29 B. Chen, C. Peng, R. Guo, Z. He, L. Sun, F. Zhang, X. He, H. Zeng and L. Wang, Dual-function self-assembled molecules

as hole-transport layers for thermally evaporated high-efficiency blue perovskite light-emitting diodes, *Adv. Mater.*, 2025, **37**, 2411451.

30 J. Zhu, J. Li, Y. Huang, N. Liu, L. Sun, Z. Shen, C. Yang, F. Liu, B. Song, J. Luo and J. Tang, All-thermally evaporated blue perovskite light-emitting diodes for active matrix displays, *Small Methods*, 2024, **8**, 2300712.

31 J. Luo, J. Li, L. Grater, R. Guo, A. R. b. Mohd Yusoff, E. Sargent and J. Tang, Vapour-deposited perovskite light-emitting diodes, *Nat. Rev. Mater.*, 2024, **9**, 282–294.

32 F. Qin, H. Tian, M. Yan, Y. Fang and D. Yang, Cesium-lead-bromide perovskites with balanced stoichiometry enabled by sodium-bromide doping for all-vacuum deposited silicon-based light-emitting diodes, *J. Mater. Chem. C*, 2021, **9**, 2016–2023.

33 Y. Chen, R. Wang, G. Kusch, B. Xu, C. Hao, C. Xue, L. Cheng, L. Zhu, J. Wang, H. Li, R. A. Oliver, N. Wang, W. Huang and J. Wang, All-site alloyed perovskite for efficient and bright blue light-emitting diodes, *Nat. Commun.*, 2025, **16**, 3254.

34 J. Park, H. Cho, J. Kim, Y. C. Huang, N. Kim, S. Park, Y. Kim, S. Lee, J. Kwon, D. C. Lee and B. Shin, Efficient and spectrally stable pure blue light-emitting diodes enabled by phosphonate passivated $CsPbBr_3$ nanoplatelets with conjugated polyelectrolyte-based energy transfer layer, *EcoMat*, 2024, **6**, e12487.

35 J. J. Do and J. W. Jung, Strategic buried defect passivation of perovskite emitting layers by guanidinium chloride for high-performance pure blue perovskite light emitting diodes, *Small*, 2024, **20**, 2400544.

36 M. V. Kovalenko, L. Protesescu and M. I. Bodnarchuk, Properties and potential optoelectronic applications of lead halide perovskite nanocrystals, *Science*, 2017, **358**, 745–750.

37 K. J. Kim, S. Kang and T. Kim, Deterioration of Li-doped phenanthroline-based charge generation layer for tandem organic light-emitting diodes, *J. Inf. Disp.*, 2025, **26**, 9–18.

38 X.-L. Wang, Y.-Q. Chen, Q. Gao, H.-Y. Lin, G.-C. Liu, J.-X. Zhang and A.-X. Tian, Coordination behavior of 5, 6-substituted 1, 10-phenanthroline derivatives and structural diversities by coligands in the construction of lead (II) complexes, *Cryst. Growth Des.*, 2010, **10**, 2174–2184.

39 Z. Q. Gao, M. Luo, X. H. Sun, H. L. Tam, M. S. Wong, B. X. Mi, P. F. Xia, K. W. Cheah and C. H. Chen, New host containing bipolar carrier transport moiety for high-efficiency electrophosphorescence at low voltages, *Adv. Mater.*, 2009, **21**, 688–692.

40 X. Shen, K. Kang, Z. Yu, W. H. Jeong, H. Choi, S. H. Park, S. D. Stranks, H. J. Snaith, R. H. Friend and B. R. Lee, Passivation strategies for mitigating defect challenges in halide perovskite light-emitting diodes, *Joule*, 2023, **7**, 272–308.

41 M. Knezevic, V.-D. Quach, I. Lampre, M. Erard, P. Pernot, D. Berardan, C. Colbeau-Justin and M. N. Ghazzal, Adjusting the band gap of $CsPbBr_{3-y}X_y$ (X= Cl, I) for optimal interfacial charge transfer and enhanced photocatalytic hydrogen generation, *J. Mater. Chem. A*, 2023, **11**, 6226–6236.

42 P. Du, J. Li, L. Wang, L. Sun, X. Wang, X. Xu, L. Yang, J. Pang, W. Liang, J. Luo, Y. Ma and J. Tang, Efficient and large-area all vacuum-deposited perovskite light-emitting diodes via spatial confinement, *Nat. Commun.*, 2021, **12**, 4751.

43 F. Ye, H. Zhang, P. Wang, J. Cai, L. Wang, D. Liu and T. Wang, Spectral tuning of Efficient $CsPbBr_xCl_{3-x}$ blue light-emitting diodes via halogen exchange triggered by benzenesulfonates, *Chem. Mater.*, 2020, **32**, 3211–3218.

44 S. Lee, J. Kim, H. Kim, C. Kim, S. Kim, C. Kim, H. Lee, B. Choi, C. Muthu, T. Kim, J. Lee, S. Lee, H. Ihee and J.-Y. Lee, Brightening deep-blue perovskite light-emitting diodes: A path to Rec. 2020, *Sci. Adv.*, 2024, **10**, eadn8465.

45 C. Ma, M.-C. Kang, S.-H. Lee, S. J. Kwon, H.-W. Cha, C.-W. Yang and N.-G. Park, Photovoltaically top-performing perovskite crystal facets, *Joule*, 2022, **6**, 2626–2643.

46 B. Hajduk, H. Bednarski and B. Trzebicka, Temperature-dependent spectroscopic ellipsometry of thin polymer films, *J. Phys. Chem. B*, 2020, **124**, 3229–3251.

47 L. T. Roling and F. Abild-Pedersen, Structure-sensitive scaling relations: Adsorption energies from surface site stability, *ChemCatChem*, 2018, **10**, 1643–1650.

48 A. Treglia, F. Ambrosio, S. Martani, G. Folpini, A. J. Barker, M. D. Albaqami, F. De Angelis, I. Poli and A. Petrozza, Effect of electronic doping and traps on carrier dynamics in tin halide perovskites, *Mater. Horiz.*, 2022, **9**, 1763–1773.

49 Y. Jiang, M. Cui, S. Li, C. Sun, Y. Huang, J. Wei, L. Zhang, M. Lv, C. Qin, Y. Liu and M. Yuan, Reducing the impact of Auger recombination in quasi-2D perovskite light-emitting diodes, *Nat. Commun.*, 2021, **12**, 336.

50 J. Li, P. Du, S. Li, J. Liu, M. Zhu, Z. Tan, M. Hu, J. Luo, D. Guo, L. Ma, L. Gao, G. Niu and J. Tang, High-throughput combinatorial optimizations of perovskite light-emitting diodes based on all-vacuum deposition, *Adv. Funct. Mater.*, 2019, **29**, 1903607.

51 H. Cho, J. S. Kim, C. Wolf, Y.-H. Kim, H. J. Yun, S.-H. Jeong, A. Sadhanala, V. Venugopalan, J. W. Choi, C.-L. Lee, R. H. Friend and T.-W. Lee, High-efficiency polycrystalline perovskite light-emitting diodes based on mixed cations, *ACS Nano*, 2018, **12**, 2883–2892.

52 H. Kwon, J. W. Lim, J. Han, L. N. Quan, D. Kim, E.-S. Shin, E. Kim, D.-W. Kim, Y.-Y. Noh, I. Chung and D. H. Kim, Towards efficient and stable perovskite solar cells employing non-hygroscopic F4-TCNQ doped TFB as the hole-transporting material, *Nanoscale*, 2019, **11**, 19586–19594.

53 Q. Li, Y. Guo, J. Lan, Y. Yang, D. Wu and Z. Bin, Spirobifluorene-based hole-transporting materials for RGB OLEDs with high efficiency and low efficiency roll-off, *Chem. Sci.*, 2024, **15**, 16096–16102.

54 Y. Noguchi, A. Hofmann and W. Brütting, Controlling charge accumulation properties of organic light-emitting diodes using dipolar doping of hole transport layers, *Adv. Opt. Mater.*, 2022, **10**, 2201278.

55 L. Zhang, X. Yang, Q. Jiang, P. Wang, Z. Yin, X. Zhang, H. Tan, Y. Yang, M. Wei, B. R. Sutherland, E. H. Sargent and J. You, Ultra-bright and highly efficient inorganic based

perovskite light-emitting diodes, *Nat. Commun.*, 2017, **8**, 15640.

56 W. Jin, Y. Deng, B. Guo, Y. Lian, B. Zhao, D. Di, X. Sun, K. Wang, S. Chen, Y. Yang, W. Cao, S. Chen, W. Ji, X. Yang, Y. Gao, S. Wang, H. Shen, J. Zhao, L. Qian, F. Li and Y. Jin, On the accurate characterization of quantum-dot light-emitting diodes for display applications, *npj Flexible Electron.*, 2022, **6**, 35.

57 J. Liang, X. Hu, C. Wang, C. Liang, C. Chen, M. Xiao, J. Li, C. Tao, G. Xing, R. Yu, W. Ke and G. Fang, Origins and influences of metallic lead in perovskite solar cells, *Joule*, 2022, **6**, 816–833.

58 X. Li, D. Luo, P. B. Green, C. Qiu, M. Wei, H. Yu, E. H. Sargent, M. W. Wilson and Z. H. Lu, Vapor-phase deposition of highly luminescent embedded perovskite nanocrystals, *Adv. Opt. Mater.*, 2022, **10**, 2102809.